Geomorphology 186 (2013) 12–27

Contents lists available at SciVerse ScienceDirect

Geomorphology

journal homepage: www.elsevier.com/locate/geomorph

# Image-based mapping of surface fissures for the investigation of landslide dynamics

André Stumpf [a,b,c], Jean-Philippe Malet [b,*], Norman Kerle [c], Uwe Niethammer [d], Sabrina Rothmund [d]

[a] Laboratoire Image, Ville, Environnement, CNRS ERL 7230, University of Strasbourg, France
[b] Institut de Physique du Globe de Strasbourg, CNRS UMR 7516, University of Strasbourg, France
[c] Faculty of Geo-Information Science and Earth Observation, ITC, University of Twente, Enschede, The Netherlands
[d] Institut für Geophysik, University of Stuttgart, Stuttgart, Germany

ARTICLE INFO

*Article history:*
Received 22 February 2012
Received in revised form 17 September 2012
Accepted 11 December 2012
Available online 22 December 2012

*Keywords:*
Landslide
Fissure
Geomorphological mapping
Remote sensing
Image filtering
UAV

ABSTRACT

The development of surface fissures is an important indicator for understanding and forecasting slope movements. Landslide investigations therefore frequently include the elaboration and interpretation of maps representing their spatial distribution, typically comprising intensive field work and instrumentation. It is only recently that aerial photography with sub-decimetre spatial resolution is becoming more commonly available and opens a window to analyse such features from a remote sensing perspective. While these data are in principle helpful to elaborate maps from image interpretation techniques, there is still no image processing technique available to extract efficiently these geomorphological features. This work proposes a largely automated technique for the mapping of landslide surface fissures from very-high resolution aerial images. The processing chain includes the use of filtering algorithms and post-processing of the filtered images using object-oriented analysis. The accuracy of the resulting maps is assessed by comparisons with several expert maps in terms of affected area, fissure density and fissure orientation. Under homogenous illumination conditions, true positive rates up to 65% and false positive rates generally below 10% are achieved. The resulting fissure maps provide sufficient detail to infer mechanical processes at the slope scale and to prioritize areas for more detailed ground investigations or monitoring.



## 1. Introduction

Observations of features and structural patterns of earth surface landforms can reveal information on the origin and mechanisms controlling the geomorphological processes. Structural geology and geomorphology have developed comprehensive concepts to delineate geomorphological units and structure types from remote sensing images, and infer about mechanical processes without necessarily measuring displacement, deformation or the applied forces directly (Melton, 1959; Davis and Reynolds, 1996; Passchier and Trouw, 2005; Pollard and Fletcher, 2005). Surface discontinuities observed in rocks and sediments have proven to be valuable indicators of the deformation history and stress pattern of the slope. For landslide analysis, their observation and interpretation can contribute to a better understanding of the controlling physical processes and help in the assessment of the related hazards (McCalpin, 1984; Fleming and Johnson, 1989; Parise, 2003). In hard-rock slopes, the analysis of structural discontinuities (faults, bedding planes, joints, and fractures) allows us to characterize potentially unstable areas (Hoek and Bray, 1981; Matheson, 1983; Priest, 1993; Selby, 1993; Günther et al., 2004; Jaboyedoff et al., 2004; Glenn et al., 2006). In soft-rock slopes and sediments, the analysis of surface fissures may indicate the development of future failures (Krauskopf et al., 1939; Shreve, 1966; Chowdhury and Zhang, 1991; Abramson et al., 2001; Khattak et al., 2010) and is often considered as a geo-indicator of the activity stage of a landslide. In sediments, the surface fissure characteristics also influence water infiltration and drainage, which in turn affect the ground-water system and the kinematic response of slopes to hydrological events (Malet et al., 2003, 2005a; van Asch et al., 2009).

Maps of surface deformation features can be obtained by extensive field surveys either through the direct visual observation of the topography (Fleming et al., 1999; Meisina, 2006) or through the indirect measure of seismic wave propagation in tomography setups (Grandjean et al., 2011; Bièvre et al., 2012). Relatively large fissures on landslides may also be discernible in Very-High-Resolution (VHR) spaceborne images (Glenn et al., 2006; Youssef et al., 2009), but typically, those structures reach widths in the decimetre-range and at present only airborne photographs provide sufficient detail for their detection in the centimetric range. Recent studies (Eisenbeiss, 2009; Niethammer et al., 2011a) have shown that VHR images acquired from unmanned aerial vehicles (UAVs) are cost-efficient data sources for the monitoring of landslide surfaces with sub-decimetric image resolution. Especially small UAVs with payloads below 5 kg and operating altitudes below 2000 m are expected to be employed much more frequently in coming years (Frost and Sullivan Co., 2007) though more specific regulations for their operational use are being discussed at national and international levels (Prats et al., 2012; Watts et al., 2012).

Visual interpretation of VHR imagery is a classical method in geomorphology, but it remains subjective, and rather impractical for

* Corresponding author.
*E-mail address:* jeanphilippe.malet@unistra.fr (J.-P. Malet).

0169-555X/$ – see front matter © 2012 Elsevier B.V. All rights reserved.
http://dx.doi.org/10.1016/j.geomorph.2012.12.010

repetitive observations or the inspection of large areas. An increasing number of studies therefore targeted the development of automated techniques to extract relevant features from imagery (Graham et al., 2010; Martha et al., 2010; Stumpf and Kerle, 2011). Although the detection and extraction of linear features is a fundamental operation in digital image processing (Quackenbush, 2004; Mendonca and Campilho, 2006; Papari and Petkov, 2011), relatively few studies have explored the application of automatic approaches for the mapping of geomorphologically relevant linear features (Baruch and Filin, 2011; Shruthi et al., 2011).

Considering the increasingly widespread availability of sub-decimetre resolution images from UAVs and other airborne platforms, this study targeted the development of a semi-automatic image analysis technique to support geomorphologists in the detection, mapping and characterization of landslide surface fissures from VHR aerial images. In this context, the term "semi-automatic" expresses that the technique requires user input to be adapted for different image types and environmental settings. The developed method is based on a combination of Gaussian directional filters, mathematical morphology and object-oriented image analysis (OOA) and was tested on a set of multi-temporal VHR images acquired at the Super-Sauze landslide (southeast French Alps). The obtained results were compared to manual mappings carried out by experts combining image interpretation and field surveys.

## 2. Types of surface fissure observed on landslides

Detailed observations of landslide surface fissures were provided by Krauskopf et al. (1939) who adapted analogies from structural geology for their interpretation and distinguished between strike–slip structures, normal faults, graben structures and compression structures. In addition, Ter-Stephanian (1946) noticed the mechanical significance of surface fissures and elaborated a classification scheme relating fissure morphology and location within the landslide mass to corresponding mechanical processes. This included a first-order differentiation between upper extension, side friction, central compression, and lower creep-on cracks. Although some authors used similar classification schemes (Bombard, 1968), the adopted terminology varies among different authors and affected lithologies (Fleming and Johnson, 1989; Cruden and Varnes, 1996; Fleming et al., 1999; Walter et al., 2009), and the terms crack and fissure are often used synonymously to refer to a variety of surface discontinuities.

Here, *fissure* is adopted as a generic term for open fractures on the topographic surface of a natural slope. At first instance, *transversal*, *longitudinal and diagonal fissures* are distinguished according to their main orientation axes relative to the dip of the slope. This terminology can be used ad hoc to classify fissures solely based on geometric properties observed in the field or in an image. A more refined mechanical classification such as provided in Ter-Stephanian (1946) will generally require considerations of the fissure patterns, the involved material and the local geometry of the slip surface. The term *crack* is used in this manuscript when referring to genetic processes described within classical fracture mechanics (Anderson, 2005). It should be noted that the term *crack* is also often adopted to refer to shrinking–swelling induced fractures (Malet et al., 2003) which are not the objective of this study.

Classical fracture mechanics postulates tensile opening, sliding and tearing as the three basic modes for crack propagation (Fig. 1a). The concept has been developed for brittle material but is also adopted to explain fracturing of plastic materials at high deformation rates (Schulson and Duval, 2009). Surface fissures may develop from a combination of all three modes, whereas in practice, considering the relatively low tensile fracture toughness of most geomaterials (Backers, 2004; Ke et al., 2008; Schulson and Duval, 2009), tensile fracturing can be expected to dominate the formation of fissures at the free surfaces of a landslide. However, interpreting tension cracks as a direct indicator for a purely tensile stress regime may often fall too short. In fact, tensile fracturing may also result from relaxation of tensile stresses that originate from deformation induced by shearing and compression as well (Wang and Shrive, 1995). A mechanical interpretation and classification of the fissures must therefore consider the fissure pattern, material and landslide geometry.

Fig. 1b–d illustrates three typical fissure patterns that are frequently used as geoindicators of specific deformation processes in the above-cited studies. One commonly observed example for such patterns is the formation of en-echelon fissure arrays (Fig. 1c), often also termed *Riedel* shears (Riedel, 1929). They accommodate tensile stress and shear stress typically resulting from shear in the bounding zone of blocks moving with different displacement rates. Certain patterns such as arrays of transversal fissures (Fig. 1b) are typically associated with tension in the steeper upper slopes, whereas fissures resulting from compression and lateral extension (Fig. 1d) are more typically associated with gentler slopes in the transit and accumulation zones of landsides (Sowers and Royster, 1978). For landslides with a complex geometry, the position of those fissure patterns may however deviate considerably from this simple scheme (Niethammer et al., 2011a).

## 3. Study site and data

The Super-Sauze mudslide is an active slow-moving landslide located in the Barcelonnette Basin in the Southern French Alps (Fig. 2) that developed in weathered black marls in the 1960s, and features highly variable displacement rates (from 0.01 to 0.40 $m \cdot day^{-1}$) controlled by the local hydrological conditions (Malet et al., 2005a). The landslide measures 950 m from the main scarp to the toe, and is up to 150 m wide. The moving mass has a clay-rich matrix containing up to 30% coarse gravel as well as larger boulders and blocks (Malet et al., 2005a). The surface displays the signs of deformation in the form of ridges, bulges, lobes and fissures but also markers of surface erosion such as rills and small gullies. Unlike surrounding stable areas the landslide surface is largely bare and only at a few locations, especially at its toe, cushion plants form small vegetation patches. Fissure widths of 0.01–0.40 m, lengths of more than 1.0 m and depths of up to 1.5 m (Espinosa, 2009) can be observed in the field (Fig. 4b). During the last 15 years, the landslide has been investigated through numerous monitoring campaigns including in-situ geophysical measurements, terrestrial and airborne LiDAR (light detection and ranging) and the acquisition of VHR optical imagery. In the VHR airborne optical images, the fissures can be recognized as dark curvilinear structures (Fig. 2c–e) as soon as their width approaches one pixel in size. Previous studies (Malet, 2003; Niethammer et al., 2011a; Walter et al., 2012) already discussed relationships between the observed fissure patterns (Fig. 2c–e) and strain resulting from a spatially heterogeneous displacement field and interactions between moving mass and the stable bedrock. However, a full reconstruction of the complex bedrock geometry that may allow for a more detailed characterisation of the underlying deformation mechanisms has been conducted only recently (Travelletti and Malet, 2012).

### 3.1. Airborne acquisitions of VHR optical imagery at the Super-Sauze landslide

Between April 2007 and October 2009, diverse imaging systems and airborne platforms were used to acquire VHR images of the landslide at five different dates (Fig. 3). In July 2008, October 2008, and October 2009, a low-cost UAV system equipped with compact camera was operated at flight heights between 100 and 250 m yielding images of the surface with a ground resolution between 0.03 and 0.10 m. The individual images were corrected for barrel lens distortion, rectified according to ground control points (GCPs) measured with differential GPS (DGPS), and finally merged into one large orthomosaic. Further details on the image acquisition and processing were provided by Niethammer et al. (2010, 2011b) who quantified

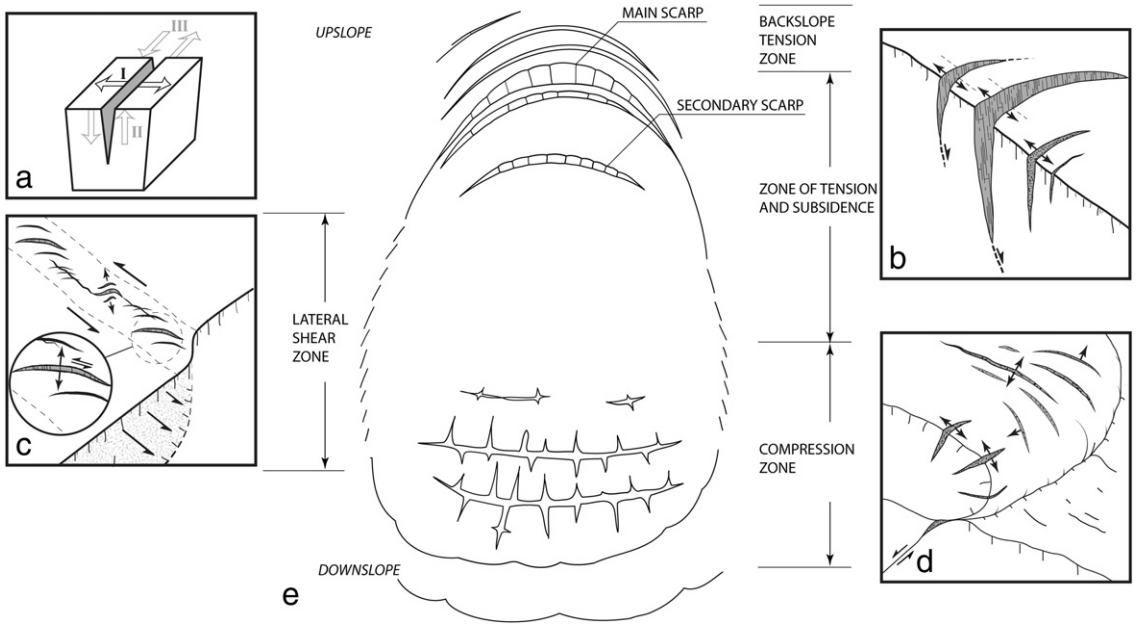


**Fig. 1.** Generic types of surface fissures and their typical spatial occurrence within a landslide mass. (a) Modes of fracture propagation: mode I (opening), mode II (sliding) and mode III (tearing). (b) Fissures developing predominately in mode I and resulting from tensile stress. (c) Fissures developing predominately in mode I and resulting from shear stress. (d) Fissures developing predominantly in mode I resulting from compressive stress and lateral expansion. (e) Division of a landslide mass (Sowers and Royster, 1978).

the residual positional error ($x$–$y$) for the October 2008 images with $0.5 \pm 0.57$ m within the boundaries of the sliding area. The UAV images for July 2008 and October 2009 are expected to provide better positional accuracies because they were orthorectified using elevation models that were generated from a photogrammetric analysis of the images.

During the two airborne LiDAR surveys in May 2007 and July 2009 (see Section 3.2), two orthomosaics of optical images with full coverage of the landslide were recorded using medium format cameras (Fig. 3) mounted on, respectively an airplane and a helicopter. The surveys used fully integrated systems for direct georeferencing and orthorectification with LiDAR surface models (see Section 3.2),

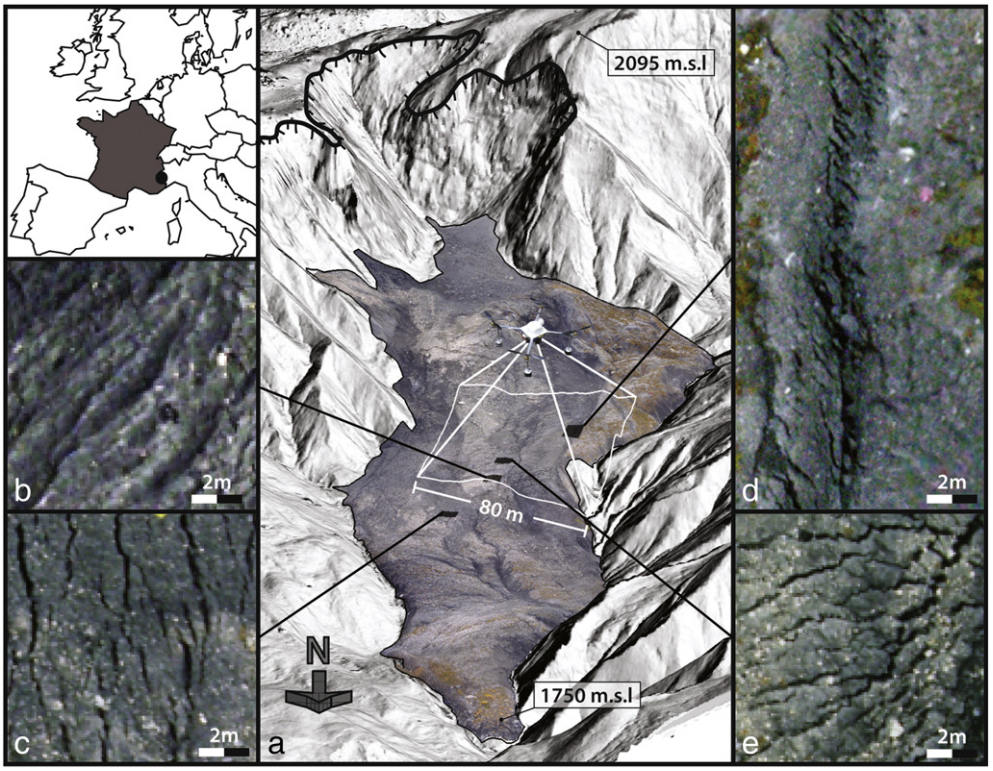


**Fig. 2.** Oblique view of the Super-Sauze landslide combining a hillshade image derived from an airborne LiDAR DTM (July 2009) and a UAV image (October 2008). (a) Main scarp (hashed black line), transport and accumulation zone (black outline), and area of interest for the multi-temporal analysis (white square). UAV image subsets show (b) compression ridges, (c) longitudinal fissures, (d) diagonal fissures at the boundary of the active part, and (e) and transversal fissures.

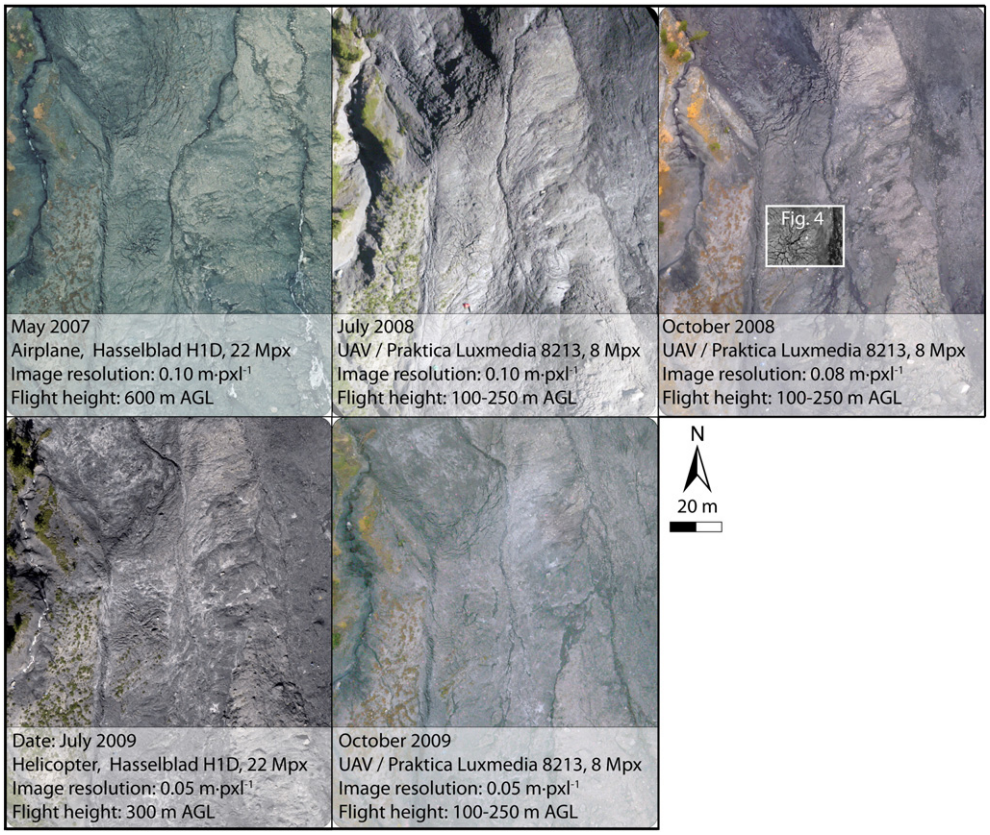


**Fig. 3.** Subsets of orthophotographs (see location in the white bounding box in Fig. 2a) acquired at five different dates with details of the acquisition systems and image ground resolutions.

which in general provide sub-decimetre positional accuracy in the *x*–*y* plane (Vallet, 2007).

For the study presented here, additionally 60 homologous tie points on stable areas were manually selected in the available images and showed a mean relative alignment error of $0.76 \pm 0.82$ m among the different acquisitions.

Further details on the adopted camera systems and the resolutions of the images resulting from the five surveys are summarized in Fig. 3. The figure also illustrates the considerable radiometric differences among the five images originating from illumination changes, seasonal variations and the distinct characteristics of the sensors. The scenes for May 2007, October 2008 and October 2009 were acquired under cloudy conditions with diffuse sky radiation and consequently show a more homogenous illumination of the surface. The scenes for July 2008 and July 2009 in contrast were recorded under sunny sky yielding strong contrast and many cast shadows. The latter are more prominent in the image for July 2008 which was recorded in the morning hours, at a relatively low sun angle. Although available methods for absolute and relative radiometric correction can be employed for the radiometric alignment of satellite images (Hong and Zhang, 2008; Vicente-Serrano et al., 2008), to the best of our knowledge, no approach exists to accurately align the radiometry of sub-decimetre images from different sensors, with substantial changes in illumination, a complex topography and changing surface characteristics. Initial test using histogram-matching, linear-regression (Schott et al., 1988) and iteratively re-weighted regression (Canty and Nielsen, 2008) did not provide satisfactory results. Consequently, no radiometric normalization was performed and the image analysis technique was designed and tested with radiometric diverse imagery.

In order to calibrate adjustable parameters of the detection algorithm to the targeted fissures and the variable scene characteristics, the processing was first tested on a subset of the terrain covering ~14,000 $m^2$ in the central part of the landslide (Figs. 2a and 3). This section was characterized by different fissure patterns and recorded during all surveys (including July 2008 and October 2009 which did not yield full coverage of the surface). Subsequently, the developed workflow was applied on the full scenes for a comprehensive mapping and analysis of the fissure distribution. Corresponding results for the full extent of the Super-Sauze landslide and their mechanical significance are discussed in Section 5.2.

### 3.2. LiDAR DTM

Two airborne LiDAR surveys were conducted in May 2007 and July 2009, respectively. The first survey used a Riegl LMS-Q560 laser scanner mounted on an airplane flying 600 m above the ground and resulted in a mean point density of 0.9 pts $m^{-2}$ after vegetation filtering. The residual 3D positional error of the ground points was quantified as 0.12 m. The second survey was conducted with a Riegl Q240i laser scanner mounted on a helicopter and after vegetation filtering resulted in a mean point cloud density of 3.2 pts $m^{-2}$. The residual 3D positional error of the ground points was 0.07 m. Continuous surface rasters with a pixel size of 0.5 m were interpolated from the respective point clouds using Delaunay triangulation. The resulting surface was then adopted for the extraction of the principal hydrological drainage lines.

### 3.3. Reference datasets: expert maps of surface fissures

Reference mappings of the fissure characteristics (type and distribution) were elaborated by an expert geomorphologist familiar with the study site. The fissures were first identified on-site during a field survey carried out in October 2009 at the same time as the acquisition of the UAV images. The position of the fissures was mapped using a dGPS survey and terrestrial photographs. Then image interpretation rules were defined to identify and digitize the fissures on the images

as polyline vectors using a 2D view and at a scale of 1:250. The image interpretation rules were then applied to the four other images in order to elaborate an expert fissure map for each date. The resulting five maps were adopted as a reference to assess the performance of the semi-automatic method.

## 4. Image processing methods

While first generic edge detection operators were already proposed in the 1980s (Marr and Hildreth, 1980; Canny, 1986), the extraction of linear features from imagery remains a challenging task in many disciplines such as medical research (Mendonca and Campilho, 2006), earth science (Shao et al., 2011; Shruthi et al., 2011) or signal processing (Lampert and O'Keefe, 2011). For our focus, the specific challenges posed for an automation of fissure detection can be summarized as follows:

- The approach should be scalable to apply for variable fissure sizes and image resolutions, and as insensitive as possible to variable radiometric image characteristics;
- The technique should not respond to edges but enable the detection of dark curvilinear structures that may be oriented at any direction. Classical techniques such as Sobel operator and the Canny detectors (González and Woods, 2008) have been designed specifically for edge detection and are not directly applicable;
- The complex micro-topography, the presence of rock blocks and gravels as well as small patches of vegetation yield highly textured images. Consequently, the approach should enable us to smooth out spurious signals from the noisy background while still retaining small partially disconnected linear features of interest. Contextual scene information should be taken into account to resolve ambiguities of the local features.

Considering these challenges, a processing workflow including three main stages was developed. Firstly, a set of scalable Gaussian filters is applied to detect fissure candidates and suppress responses at edges. Secondly, a set of morphological filters is used to close small gaps along the extracted candidates. Thirdly, an object-oriented procedure is followed to eliminate some of the false positives exploiting higher-level scene information with contextual rules.

### 4.1. Stage 1: extraction of fissure candidates using a Gaussian matched filtering algorithm

A particularly well-studied example for the detection of dark curvilinear structures is the extraction of dark blood vessels in photographs of the human retina. Based on the observation that the cross-profiles of the vessels resembles a Gaussian distribution, Chaudhuri et al. (1989) proposed the use of a matched filter (MF) that is essentially a Gaussian convolution kernel subtracted by its own mean value. As illustrated in Fig. 4a, the cross-sections of surface fissures can be approximated with a Gaussian distribution and an MF scaled to the size of the fissure will give a peak response when crossing the fissure at an angle of approximately 90°. Because the MF still yields errors such as false detections at step edges (Fig. 5a, c) numerous extensions (Hoover et al., 2000; Sofka and Stewart, 2006) and alternative approaches (Mendonca and Campilho, 2006; Soares et al., 2006) have been developed. Recently, Zhang et al. (2010) proposed modification to the original MF filtering approach integrating a first order derivative of a Gaussian function (FDOG) to locally adapt the thresholds separating dark lines from non-target features. Compared to other state-of-the-art algorithms their approach provided competitive accuracies while being a computationally efficient and hence easier to apply on the large images resulting from VHR remote sensing.

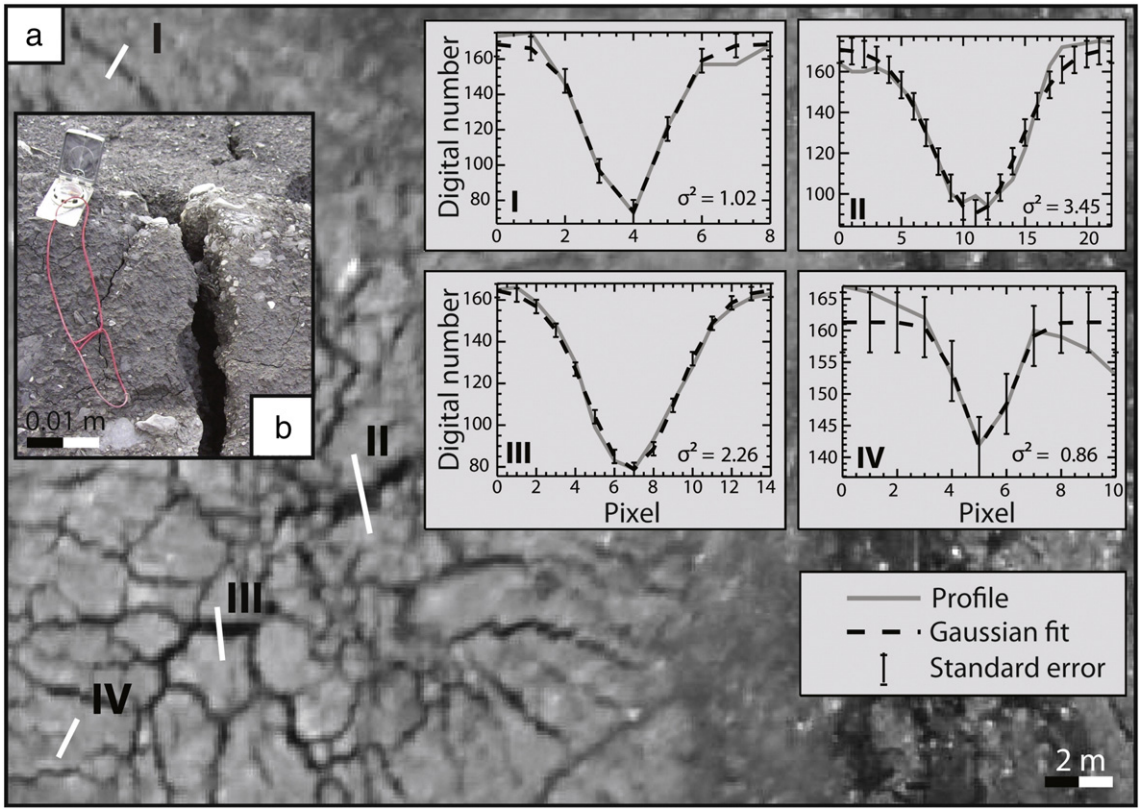


**Fig. 4.** Images of surface fissures. (a) Subset (see extent in Fig. 3) of the UAV image from October 2008 showing typical fissure patterns and (I–IV) grey-value profiles (green channel) approximated with Gaussian curves. (b) Field photograph taken in October 2009.

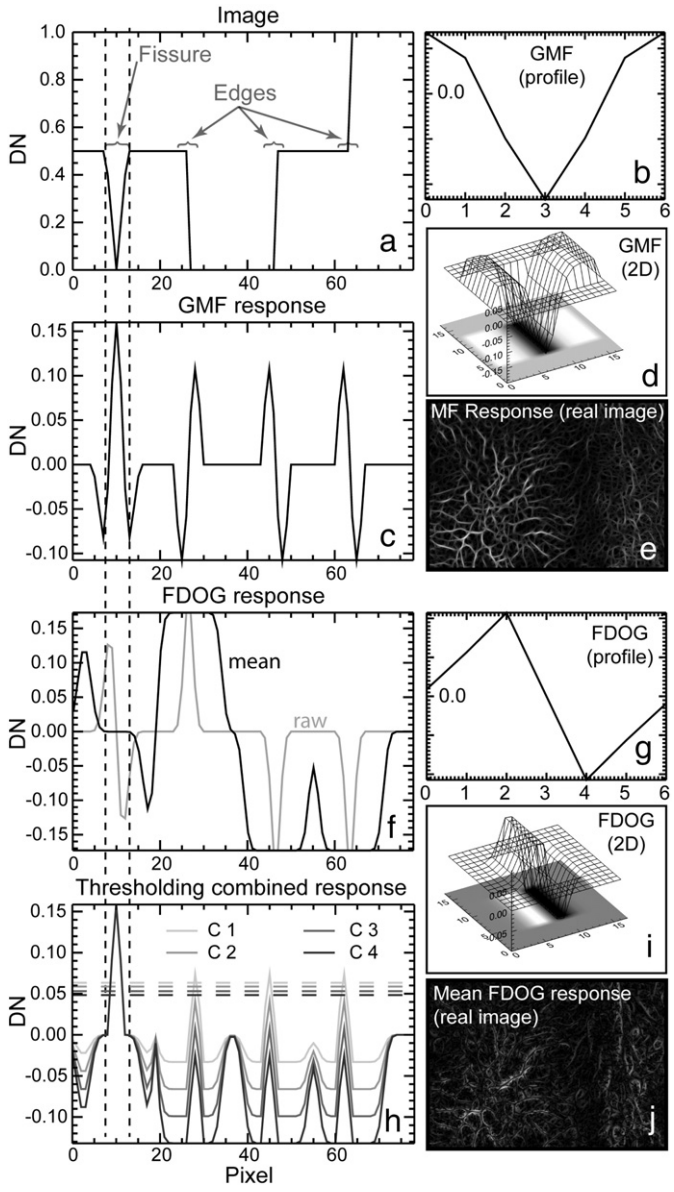


**Fig. 5.** Illustration of the principles of the Gaussian filtering for (a–c and f–h) a simplified 1-D case, (d and i) a 3D visualization of 2D filters and (e and j) the filter responses for the image subset in Fig. 4a. See text for details.

For this study, a similar approach was implemented in ENVI-IDL 4.8 (ITT Visual Information Solutions). The algorithm and its parameterization are detailed below.

The MF is a two dimensional kernel defined in the $x$-direction by an inverted Gaussian profile (Fig. 5b), and in the $y$-direction by replicates of the same profile (Fig. 5d). It may be denoted as:

$$\mathrm{MF} = g(x,y;\sigma) = -\frac{1}{\sqrt{2\pi}\sigma} e^{\left(\frac{x^2}{2\sigma^2}\right)} - m, \text{for } |x| \le 3\sigma, |y| \le L/2 \quad (1)$$

where $\sigma$ denotes the standard deviation of the Gaussian functions and relates to the width of the targeted feature. To centre the kernel on zero, it is subtracted by its own mean $m$. The extent of the kernel in the $x$-direction is typically constrained to $3\sigma$, whereas $L$ defines the extent of the kernel in the $y$-direction and can be related to the length of the fissures. Because the matched filter still yields false responses at dark and bright step edges (Fig. 5c) Zhang et al. (2010) proposed to use the response of the FDOG to locally adjust the thresholds which are applied to classify the MF response into fissure and non-fissure structures. In analogy to Eq. (1), the first order derivative filter may be denoted as:

$$\mathrm{FDOG} = g'(x,y;\sigma) = -\frac{1}{\sqrt{2\pi}\sigma^3} e^{\left(\frac{x^2}{2\sigma^2}\right)}, \text{for } |x| \le 3\sigma, |y| \le L/2 \quad (2)$$

Fig. 5f illustrates that the FDOG responds with a single peak to edges but with a zero crossing at the centre of the idealized fissure. A simple mean filter can be applied to broaden the zero crossing into a plateau covering the whole width of the fissure (Fig. 5f). Subtracting the smoothed FDOG response from the MF response will attenuate the signal at edges while at the position of the fissure the full response is retained (Fig. 5h).

Since the orientation of the fissures is a priori unknown, multiple rotated versions of the Gaussian filters are applied to the image and for each pixel only the maximum response value is retained. This corresponds to finding the angle $\theta_{\max(x,y)}$ which maximizes the filter response at a given position in the image $I_{(x,y)}$ using:

$$\theta_{\max(x,y)} = \arg\max\left(I_{(x,y)} \otimes \mathrm{MF}_{\theta}\right), \text{for } 0 < \theta_i \le \pi \quad (3)$$

where $\otimes$ denotes the convolution operator and $\theta$ the orientation of the MF.

The calculation of the maximum response image $R$ can then be obtained with:

$$R_{(x,y)} = \left[I_{(x,y)} \otimes \mathrm{MF}_{\theta\,\max(x,y)}\right] > 0 \quad (4)$$

where all negative response values are automatically set to zero and only values greater than zero are retained. The FDOG filter is rotated according to the determined $\theta_{\max(x,y)}$ and the corresponding response image $D$ can be derived by:

$$D_{(x,y)} = \left|I_{(x,y)} \otimes \mathrm{FDOG}_{\theta_{\max(x,y)}} \otimes M\right| \quad (5)$$

where $M$ denotes the above-mentioned mean filter used to broaden the zero crossing to the width of the fissures.

While Zhang et al. (2010) used a very broad mean filter with a fixed size, we suggest to use a kernel size that matches the width of the Gaussian kernel ($6\sigma$) and is thereby related to the width of the targeted features (Fig. 5a, f). In contrast to early studies where the FDOG response was used to locally adapt the threshold (Zhang et al., 2010) the final response image $\bar{R}$ is obtained by subtracting the FDOG from the GMF response using:

$$\overline{R_{(x,y)}} = R_{(x,y)} - Ct * D_{(x,y)} \quad (6)$$

where $Ct$ denotes a user defined trade off parameter to adjust the sensitivity of the detection with typical range of values between 3 and 4. A threshold $T$ is defined by:

$$T = \mu_{\bar{R}} + 2\,\sigma_{\bar{R}} \quad (7)$$

where $\mu_{\bar{R}}$ is the mean of the response image $\bar{R}$ and $\sigma_{\bar{R}}$ is the respective standard deviation.

A binary fissure candidate map $F_{\mathrm{map}}$ is obtained by applying the threshold $T$ on the response image $\bar{R}$ using:

$$\overline{R_{(x,y)}} \ge T_{(x,y)} : F_{\mathrm{map}} = 1 \text{ and } \overline{R_{(x,y)}} \mathrm{b} T_{(x,y)} : F_{\mathrm{map}} = 0. \quad (8)$$

The thresholding after subtraction of the FDOG response was found to provide a generally more robust attenuation of undesired

**Table 1**
Parameter set of the Gaussian filters scaled according to the respective image resolution.

| Image date | May 2007 | July 2008 | October 2008 | July 2009 | October 2009 |
|---|---|---|---|---|---|
| Pixel size [m] | 0.10 | 0.10 | 0.08 | 0.05 | 0.05 |
| $\sigma$ [pixel] | 0.60 | 0.60 | 0.75 | 1.20 | 1.20 |
| $L$ [pixel] | 10 | 10 | 12 | 20 | 20 |
| $n_\theta$ | 36 | 36 | 36 | 36 | 36 |
| $Ct$ | 3.0 | 3.0 | 3.0 | 3.0 | 3.0 |

edge responses than the technique previously applied by Zhang et al. (2010).

In summary, the user needs to specify four simple parameters, namely (1) the scale of the filter kernels in terms of $\sigma$, (2) the length $L$ of the kernel, (3) the constant $Ct$ of the thresholding sensitivity and (4) the number of orientations $n_\theta$ at which the filters are calculated. In this study, $n_\theta$ was kept constant at 36 for all experiments, whereas, if computational time becomes an issue, the angular resolution may be reduced to 12 steps without major losses of accuracy. To determine $\sigma$ a tool was created, which allows drawing profiles on the image and automatically estimates the fitting Gaussian function (Fig. 4). Cross-profiles of the smallest fissures visible in the image with the coarsest resolution (0.1 m pixel$^{-1}$) were best fitted by Gaussian curves with $\sigma \approx 0.6$. To ensure a homogenous scale of the detected features among all images, the kernel can be scaled by changing $\sigma$ relative to the image resolution. If, for instance, the image resolution is increased to 0.08 m pixel$^{-1}$, a value of $\sigma \approx 0.75$ yields a kernel with the same physical size (Table 1). The same applies to the filter length $L$ which was estimated at 1 m corresponding to the typical minimum length of the fissures. Resampling of the images can thereby be avoided. In our experience, $\sigma$ establishes the lower bound for the width of the targeted features, whereas the filters still remain sensitive to features which are up to 5 times larger. For the choice of $\sigma$ it is also helpful to note that the discrete kernel cannot represent FDOG functions with $\sigma \leq 0.5$.

To assess the sensitivity of the parameters and to determine a suitable threshold parameter $Ct$, a sensitivity analysis was carried out on a subset of the October 2008 image. Based on a visual assessment, values of $L =$ 1 m and $\sigma = 0.75$ were found suitable for the detection of the fine fissure structures. The preliminary analysis also showed that increasing the parameters $L$ and $\sigma$ directs the detection towards more elongated and broader features, whereas in general the sensitivity of those parameters is rather low compared to the influence of the threshold $Ct$. Values of

**Table 2**
Summary of the thresholds adopted in the object-oriented post-processing routine. See text for details.

| Feature | Thresholds |
|---|---|
| Shadow | Red $<$ 100*, 40** |
| Shadow ratio | $\leq$ 0.33 |
| Vegetation | Ratio blue $\leq$ 0.33 + Otsu |
| Relative border to vegetation | $\leq$ 0.15 |
| Minimum angular difference | $>$ 13° |
| Minimum length (clean up) | $\geq$ 0.4 m |
| Minimum area (clean up) | $>$ 0.1 m$^2$ |
| Minimum fissure density (clean up) | $>$ 1%.10 m$^{-2}$ |

* For May 2007, July 2008 and October 2008.
** For July 2009 and October 2009.

$Ct = \{0.0, 1.0, 2.0, 3.0, \text{and } 4.0\}$ were tested and based on a visual assessment of the outputs, a value of $Ct = 3$ was established for an optimal trade-off between detection rate and the amount of false positives. The final parameter set is summarized in Table 1.

### 4.2. Stage 2: connection of broken lines using structuring elements

The highly textured surface of the landslide constitutes a noisy background that affects the detection especially at section where the fissures are very thin or partially occluded. While a human operator can easily interpolate broken lines through perceptual grouping (Metzger, 1975), this needs special attention for a semi-automated mapping technique.

To close small gaps between broken line segments of the detected candidates, a hit-or-miss transform algorithm (Serra, 1982) was used. The transform assigns a value of 1 to each pixel whose local neighbourhood fulfils the criteria defined by hit-and-miss structures (Fig. 6a), also known as structuring elements. They were defined to address all plausible 3-by-3 neighbourhoods representing small gaps in the detection starting from four prototype hit-structures shown in Fig. 6b. The respective miss-structures (Fig. 6c) are typically derived by simply inverting the prototype hit-structures, and both elements were rotated (Fig. 6d) to test for a total number of 24 possible neighbourhood arrangements. Exceptional cases were thereby the structuring elements for closing directly diagonal gaps, where an extended neighbourhood was used for the hit-and-miss structures (Fig. 6b, c) to prevent connections of lines running parallel to each other.

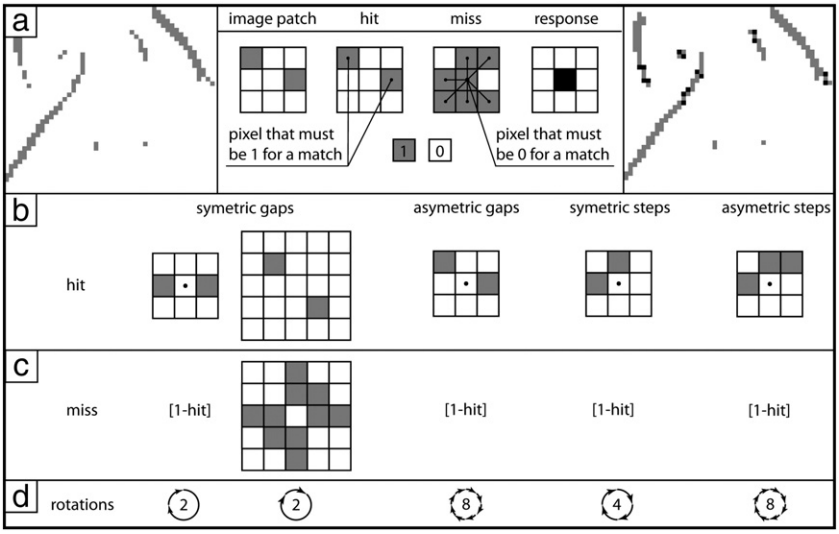


**Fig. 6.** Strategy used to connect broken line segments. (a) Working principle of the hit- and miss transform, (b) hit structures, (c) miss structures and (d) respective rotations used for the plausible pixel neighbourhoods.

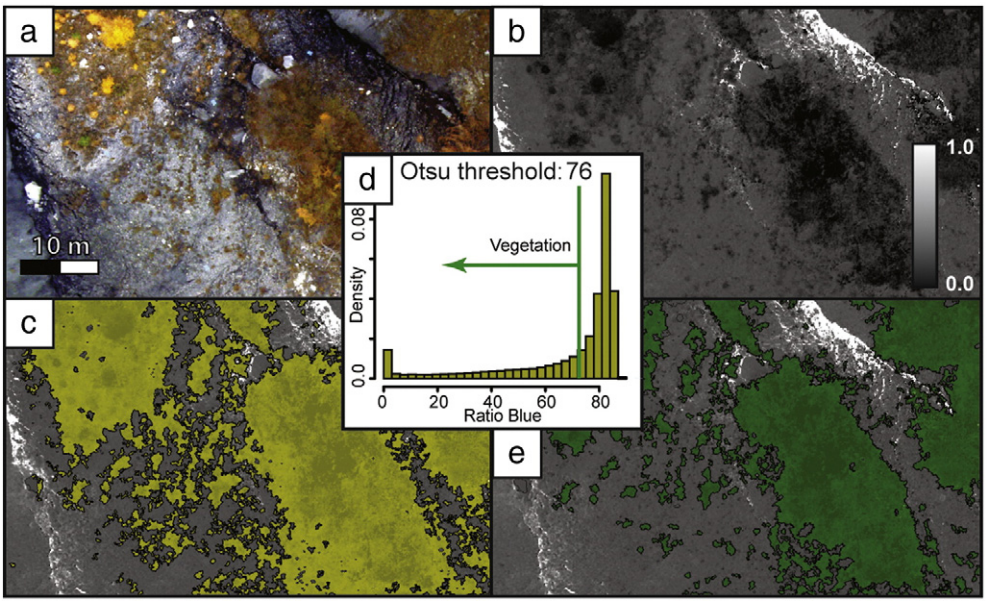


**Fig. 7.** Illustration of the automatic threshold detection for the intermediate mapping of vegetation. (a) Subset of the October 2008 image at the toe of the landslide. (b) Ratio blue. (c) Initial thresholding at ratio blue<0.33 to obtain vegetation candidates (yellow). (d) Histogram of the vegetation candidates with the automatically selected threshold. (e) Final map of the vegetation (green).

The connectivity of the line segments was also particularly important for the subsequent object-oriented post-processing, where objects constitute from pixels groups connected in a Von Neumann neighbourhood (four adjacent pixels at each side), and small isolated objects could be disregarded as noise.

### 4.3. Stage 3: object-oriented analysis for false positive removal

Due to visually similar objects, such as linear erosion features (rills and small gullies) and elongated shadows induced by the micro-topography, the fissure candidates resulting from the described filtering routine may still comprise numerous false positive detections. While a human interpreter can differentiate most of the false positives assessing the geospatial context of the scene, the efficient use of such information with automated systems is a challenge for object-oriented image analysis. To exploit the contextual scene information for an automatized refinement of the extracted fissure candidate maps, an object-oriented routine that integrates spatial reasoning into an explicit form was elaborated and implemented using eCognition 8.64 (Trimble, 2011). The routine included the following steps:

1) The ratio of shadow around the detections is evaluated and candidates with a ratio of shadow pixels in their smallest enclosing circle above 33% are regarded as false detections induced by shadings of the micro-topography. This ratio threshold was determined empirically through visual inspection of the candidate fissures, and selected to capture elongated false detections with one side lying fully in shaded zones. The threshold for shadow can thereby be adjusted according to the illumination conditions and the dynamic range of the image (Table 2).

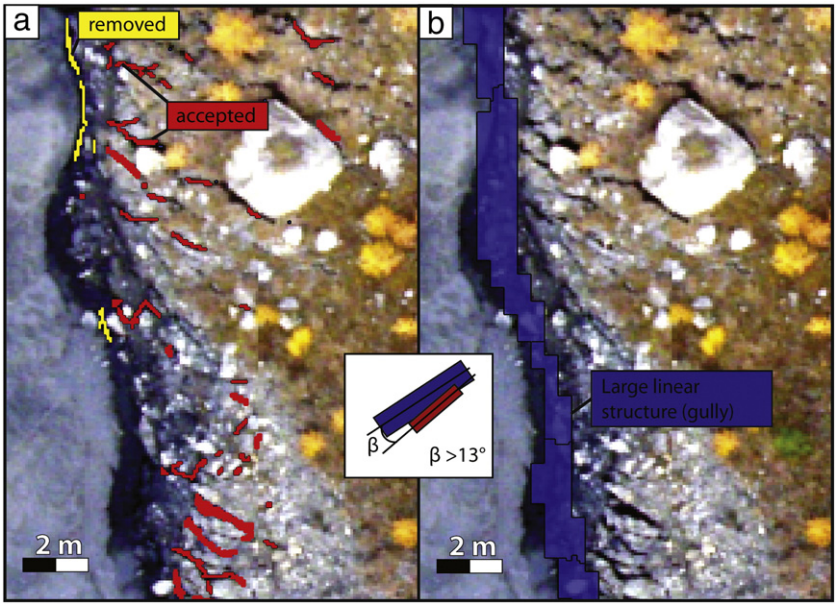


**Fig. 8.** Illustration of the object-oriented post-processing routine. (a) Fissure candidates that overlapped with linear structures. (b) Linear structure detected at a ten times greater filter scale. The fissure candidates aligned with the linear structures at angles below ±13° were removed.

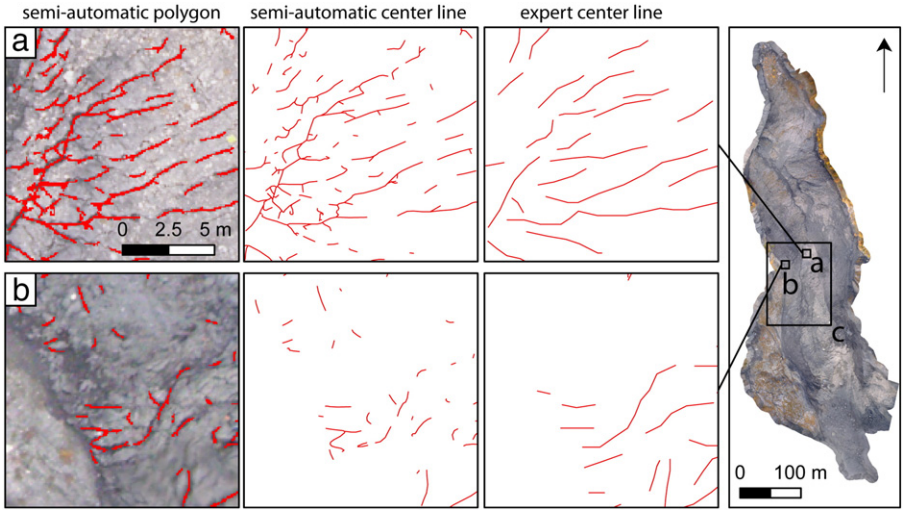


**Fig. 9.** Example of comparison of the obtained fissure maps with the expert mapping for October 2010 (fissures in red). (a) Area with relatively high agreement of the mapped fissure patterns. (b) Area with relatively high rate of false negatives and false positives. The scale of the representations corresponds approximately to the scale used for the expert mapping (1:250).

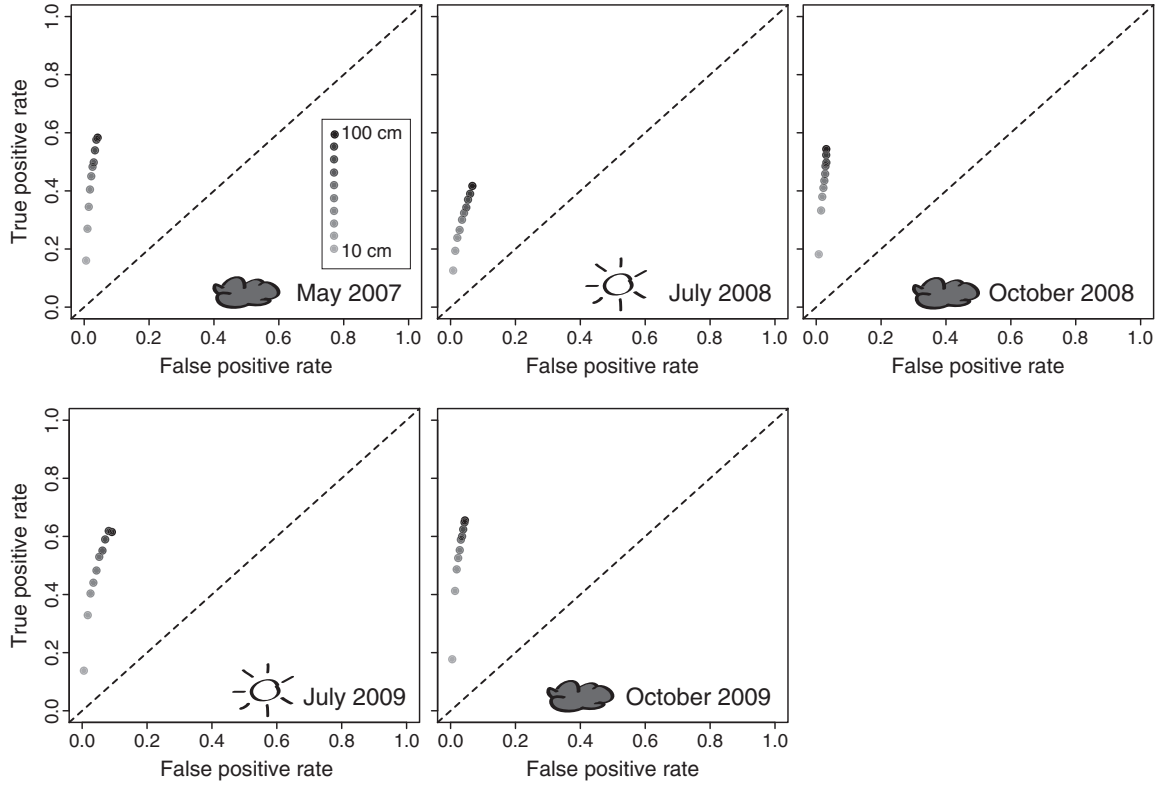


**Fig. 10.** Receiver operating characteristics (ROC) plots for the fissured area at different map resolutions. The sky conditions for the five different dates are indicated.

2) Further false detections may result from vegetation which typically shows a lower reflectance in the green and red channel compared to the blue. The blue ratio in the sum of all channels is consequently typically below one third for vegetated areas. The suitable value varies slightly with the illumination conditions and the season, and Otsu's method (Otsu, 1979) was employed to automatically adapt to such changes. Through an iterative testing of all possible values, Otsu's method determines threshold value that maximizes variance between two classes in an image. Hence, constraining the search space to all pixels with a ratio blue below 33%, the algorithm was used to determine the thresholds that maximize the contrast between vegetation and the background (Fig. 7). Fissure candidates covered by the resulting vegetation class, or having a relative border length larger than 0.15, were subsequently removed.
3) Another class of frequent false detections resulted from linear objects such as rills, gullies and nearly vertical steps at the landslide

**Fig. 11.** Correlation between fissure density estimates at 5 m raster resolution based on semi-automatic detections and expert mappings from the five images. The bar plots at the bottom display the $R^2$ coefficient at different raster resolutions.

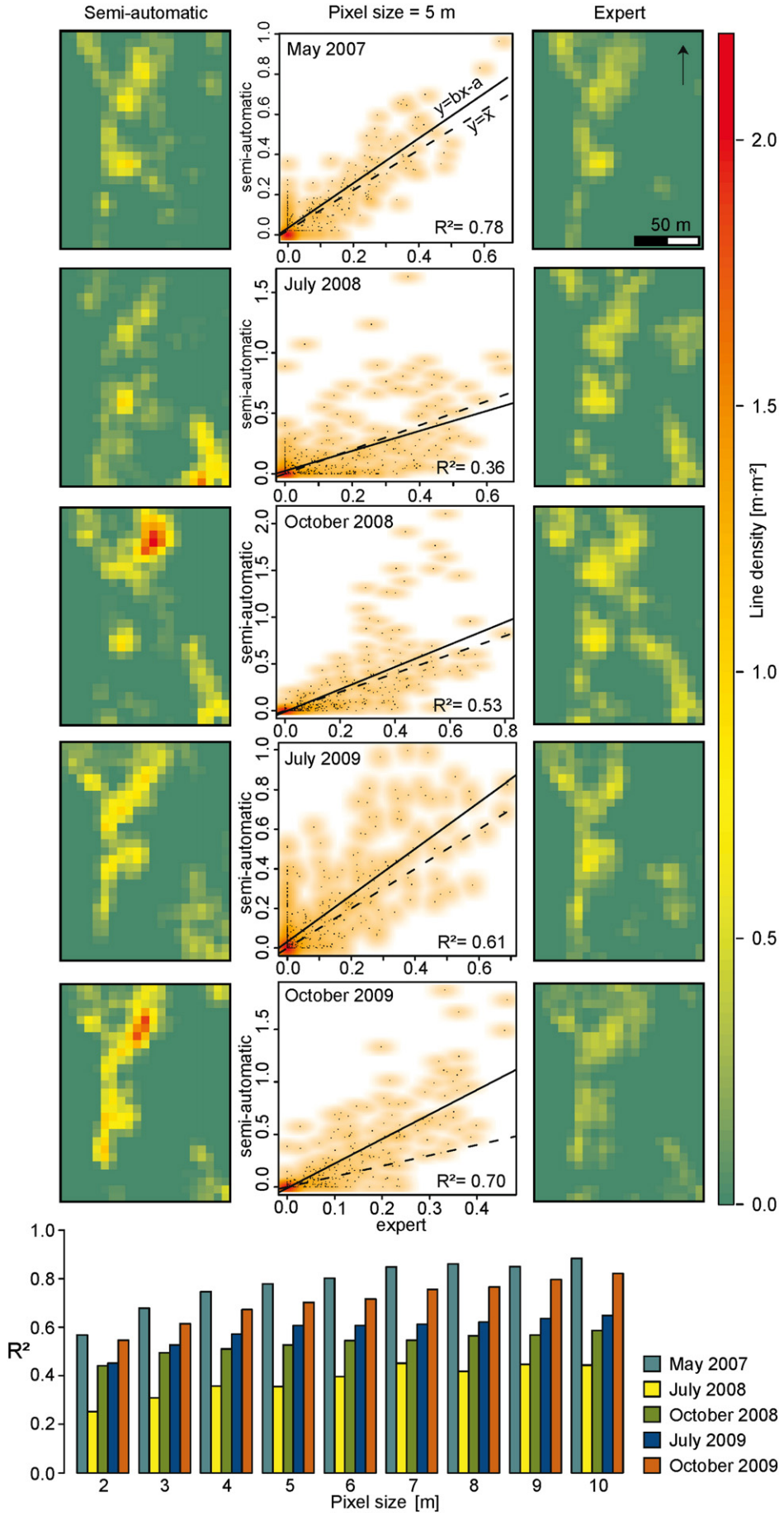
Semi-automatic
Pixel size = 5 m
Expert
May 2007
y=bx-a
y=x
R²= 0.78
50 m
July 2008
R²= 0.36
October 2008
R²= 0.53
July 2009
R²= 0.61
October 2009
R²= 0.70
semi-automatic
expert
Line density [m·m⁻²]
R²
Pixel size [m]
May 2007
July 2008
October 2008
July 2009
October 2009

flanks, which may locally obtain similar characteristics as the targeted fissures. To test for the presence of larger linear features and evaluate their relationship with fissure candidates, a strategy to suppress additional false positives was required. For the mapping of the larger linear elements, two sources were adopted. First drainage lines were extracted from the LiDAR DTMs using hydrological standard tools (Tarboton et al., 1991) and enlarged with a surrounding buffer of 0.5 m. A second approach was to repeat the Gaussian filtering with the parameter set indicated in Table 1, but with a two times increased scale $\sigma$ and a five times coarser image resolution (resampled with bilinear interpolation). This is equivalent to a search with a 10 times larger scale providing a sufficiently large scale difference to assure that none of the detected linear features would correspond to fissures. The linear objects extracted with both approaches were virtually overlaid with the fissure candidates, and the difference of the orientations of their respective centre lines was adopted as criteria to evaluate if the fissure candidate was in fact part of a larger linear object or constitutes an independent structure (Fig. 8). Image-based measurements of the angular offset of the fissured indicated a minimum offset of about $\pm 13°$. Considering that the lowest effective friction angle values measured for the landslide material are $\alpha' = 26°$ (Malet et al., 2005b), the thresholds are consistent with the orientation of $\alpha'/2$ that the Coulomb criterion predicts for the orientation of shear fissures at the landslide boundary (Tchalenko, 1970).

4) A last filtering step was implemented by removing all candidates with length not longer than 0.4 m and an area smaller than 0.1 $m^2$. Finally, all fissure candidates falling in areas with a fissure class density lower than 1% in a surrounding neighbourhood of 10 $m^2$ were considered as noise and also removed.

Table 2 displays that most adopted thresholds were kept the same among all the images and only the classification rule for the shadow areas was adapted in order to compensate radiometric differences in the input images.

## 5. Results and discussion

### 5.1. Comparison with multi-temporal manual mappings

The primary output of the developed processing routine is a map of the detected fissures represented by polygons. Applying a Delaunay triangulation that extracts the skeleton of those polygons (Trimble, 2011), a 2D line representation, which enables a more immediate comparison with expert mappings, can be obtained.

Fig. 9 displays an example of comparison between an expert map and the result of the semi-automatic detection. A first visual assessment of the obtained maps suggested better agreement of the fissure patterns in areas with high contrast and low texture (Fig. 9a), whereas false positives and false negatives concentrated in sections with low contrast and increased surface texture (Fig. 9b).

For a quantitative assessment of the mapping accuracy, the obtained results were compared with the expert mappings in the central part of the landslide (Fig. 9c) at all five dates. While several accuracy measures for geographic line datasets have been already proposed, there is still no consensus about one generally applicable technique and the metrics should be selected according to the problem at hand (Ariza-López and Mozas-Calvache, 2012). Here, we focus on three crucial aspects of the map accuracy that may have direct implications for their further use, namely the size of the affected (e.g. fissured) area, the length and density of the fissures, and their orientation.

#### 5.1.1. Size of the fissured area

Tveite and Langaas (1999) suggested an accuracy measure for line datasets based on repeated buffering and overlay operations of detected and reference line datasets. A similar strategy was adopted in this study by repeatedly calculating true positive and false positives rates from two raster data representing the detections and the expert mapping at increasingly coarser resolutions. The raster data were calculated at 10 cm steps for resolutions between 0.1 and 1.0 m, and each pixel was assigned as fissured or non-fissured area according to the presence or absence of a fissure in the detections and the reference map, respectively. The resulting receiver operating characteristics (ROC) plots are presented (Fig. 10). The analysis showed a correspondence with the expert maps at true positive rates typically above 40% and up to 65%. The false positive rates were below 5% except for the scenes recorded with full sunlight where false positive rates up to 9% could be observed (Fig. 10).

#### 5.1.2. Fissure length and density

Hydrological models that integrate the influence of surface fissures on infiltration and preferential flow have demonstrated that the fraction of fissures per unit area is an important parameter with considerable influence on the modelled water storage (Malet et al., 2005a; Krzeminska et al., 2011). Such models are typically generated at slope scale with grid resolutions below 10 m. To assess the accuracy of the extracted maps with respect to this potential application, the fissure density was calculated as the line length in circular sliding windows with diameters between 2 and 10 m, and compared among automated detection and expert mappings.

The regression plots in Fig. 11 illustrate the correlation of the fissure density estimates with a 5 m circular sliding window yielding coefficient of determination ($R^2$) typically above 0.5. The regression analysis further indicated generally higher densities resulting from the semi-automatic detection originating from false positive detections but also from a stronger generalization of the fissure line drawings within the expert mapping. Exceptions from this general trend are the results obtained from the image of July 2008 which was recorded at a low sun incidence angle leading to a relatively low $R^2_{5m} = 0.36$. The bar plots in Fig. 11 display generally higher $R^2$ values at increasing resolutions of the density raster. This is a well-known effect of spatial aggregation on correlation statistics (Gotway and Young, 2002) but also reflects the contrast between stronger discrepancies of local details and a better correspondence of the global fissure pattern pictured in the respective maps. The highest correlation was observed among the mappings for May 2007 with $R^2_{10m} = 0.88$ indicating that the lower resolution of the corresponding input image was not an important factor for the accuracy of the detection.

#### 5.1.3. Fissure orientation

As outlined in the Introduction section, different fissure patterns may signal respective mechanical processes, and statistics of the principal fracture orientation often allow us to estimate the directions of the principal stresses (Pollard and Fletcher, 2005). The fissure orientations were quantified as a third factor to assess the accuracy of the extracted maps using rose diagrams frequently employed for the analysis and interpretation of two dimensional orientation data (Jammalamadaka and SenGupta, 2001). Rose diagrams with a bin width of 10° were computed on a 10 m regular grid for the semi-automatic detections and the expert mappings at all five dates. Considering the length and direction of each bin expressed as a respective vector the preferred fissure orientation within a grid cell can be calculated by summing the vectors over all bins. Taking into account all cells containing fissures in both the

**Fig. 12.** Rose diagram plots with mean orientation (red line) and error statistics for the mean fissure orientation per 10 m grid cell for the test area at the five different dates. For visualization, the rose diagrams where plotted over a hillshade of the landslide surface and the scatterplot angles were centred at 90°.

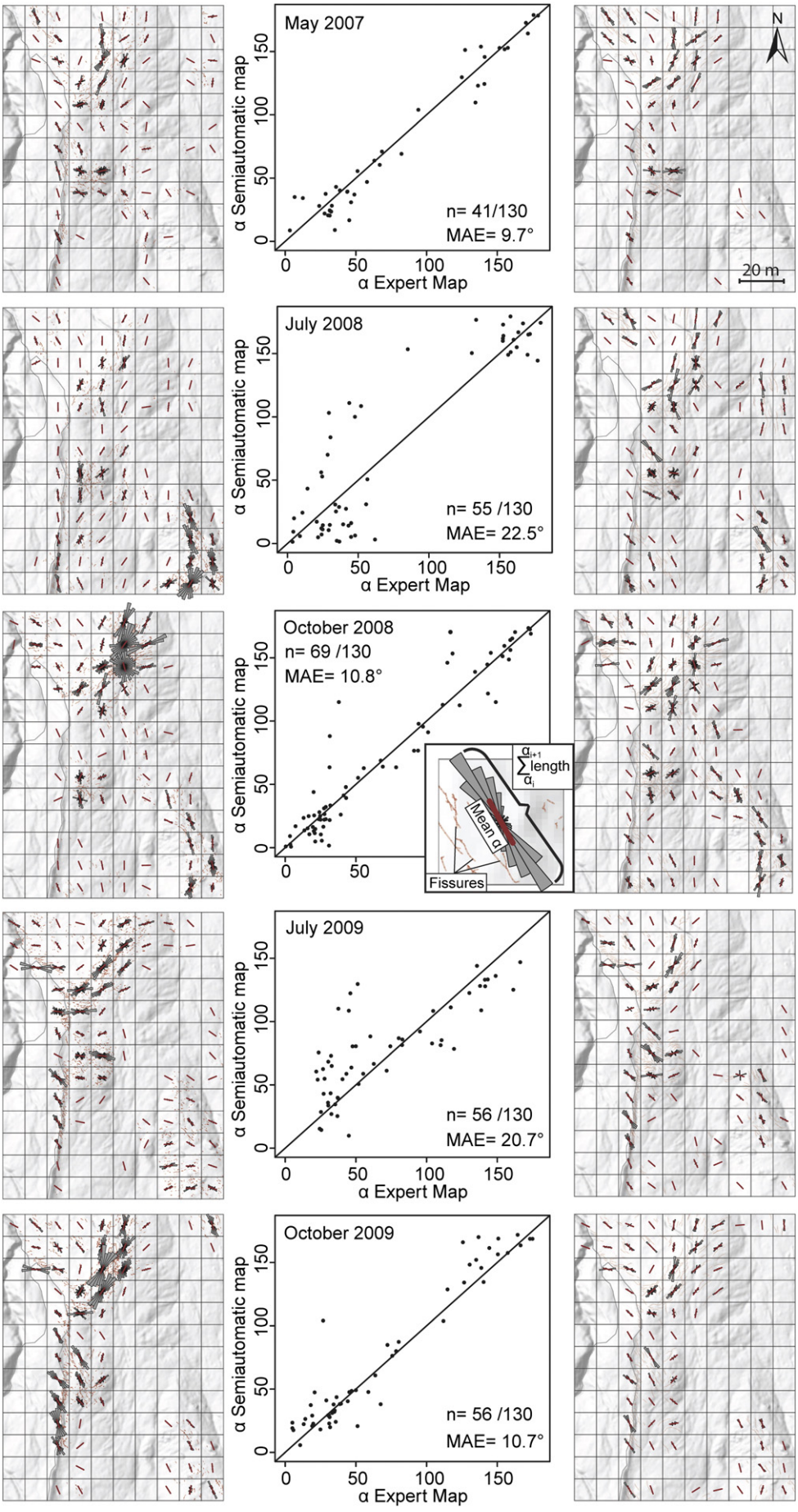
May 2007
n= 41/130
MAE= 9.7°
July 2008
n= 55 /130
MAE= 22.5°
October 2008
n= 69 /130
MAE= 10.8°
Mean α
Fissures
July 2009
n= 56 /130
MAE= 20.7°
October 2009
n= 56 /130
MAE= 10.7°
α Semiautomatic map
α Expert Map
0
50
100
150
N
20 m

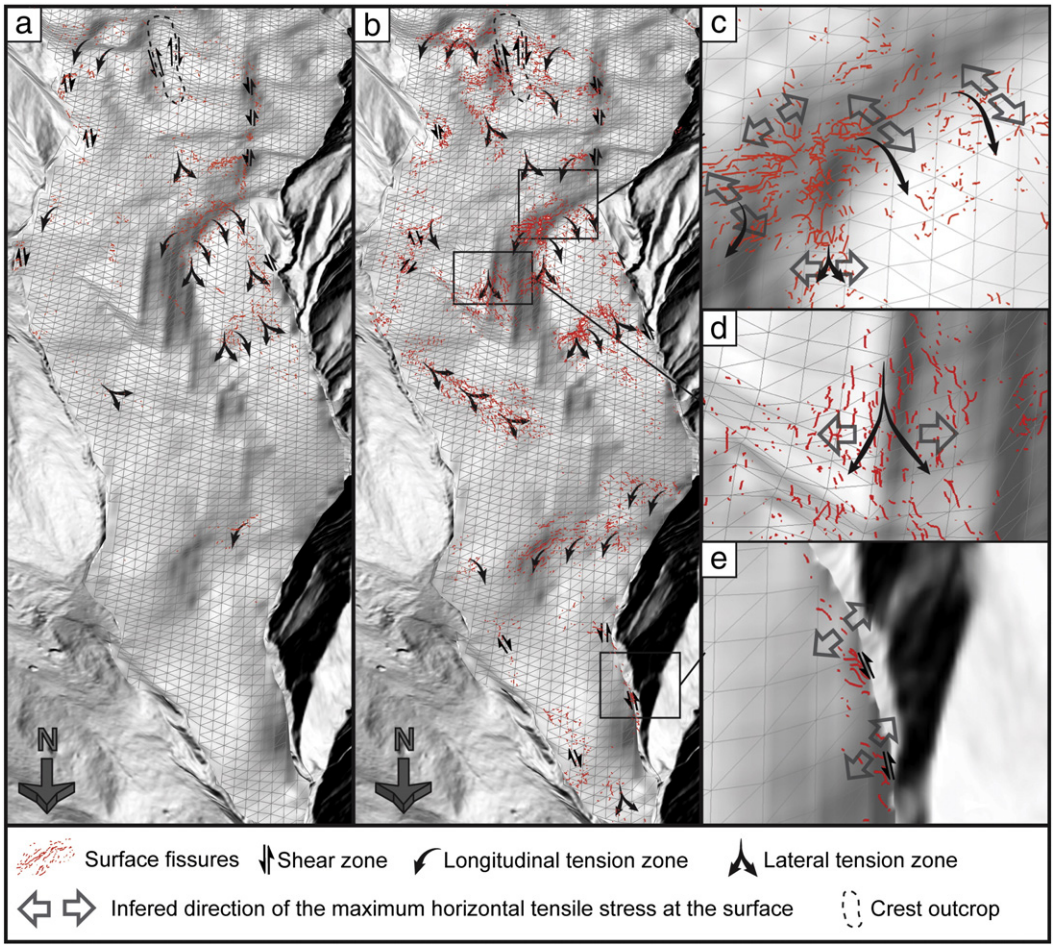


**Fig. 13.** Pseudo 3D view showing the landslide dynamics inferred from the fissure patterns detected in the aerial images of (a) May 2007 and (b) October 2008. (c, d, and e) Close up views for October 2008 showing inferred landslide dynamics and stress vectors. The results are overlaid on a hillshade model of the topography of the stable bedrock proposed by Travelletti and Malet (2012).

expert map and the semi-automatic detection, the mean absolute error (*MAE*) of the mean orientations provides a quantitative measure for the orientation accuracy.

The rose diagrams plots and error statistics in Fig. 12 depict *MAE* values between 9.7° and 22.5° for the five dates. The detections on the three scenes recorded under cloudy sky resulted in *MAE* not larger than 10.7°, whereas the error rate clearly exceeded 20° with the scenes of July 2008 and 2009 recorded with full sunlight at the surface. The lower orientation accuracies are largely consistent with the relatively low accuracies in terms of area (see Section 5.1.1) and density (see Section 5.1.2) resulting from the detection at the latter two dates.

### 5.2. Fissure patterns as possible geoindicators of deformation processes

For a comprehensive interpretation of the detected fissure patterns at the scale of the entire slope, the scenes of May 2007, October 2008 and July 2009 offering a full coverage of the landslide, have been analysed. However, considering the relatively low detection accuracy on the sunlit images of July 2009, the interpretation was focused essentially on the scenes of 2007 and 2008 spanning also over a period with displacement rates significantly above the average annual rates (Travelletti, 2011).

Comparing the detection results of May 2007 (Fig. 13a) and October 2008 (Fig. 13b), a significant increase in the abundance of fissures could be noted for the entire landslide. This can be attributed to a phase of strongly increased displacement rates (up to 3.5 m day$^{-1}$) in early June 2008 (Travelletti, 2011) preceding the UAV survey in October 2008. However, in October 2008, the displacement rates already consolidated again at average rates between 0.01 and 0.03 m day$^{-1}$, most of the fissures induced in June were preserved and evolved at the surface until October. This view is supported by the results obtained for the test area with the five scenes (Figs. 10 and 11) picturing rather a transient evolution than a complete reorganization of the fissure patterns. Despite partially strong disagreement in the absolute measured fissure density, both expert maps and semi-automatic mapping showed an increase in fissure density after May 2007, with higher values in October 2008 (Fig. 11) than directly after the peak displacement in spring. Pluviometric records for the area in 2008 show the relatively dry summer season with a cumulative rainfall of 110 mm for the month of July, August and September, suggesting that the increased fissure density in October is partially caused by an increased brittleness of the upper soil layer that dried out during summer.

Besides the general increase in the amount of fissures, it is intriguing to observe that at several local plots, similar fissure patterns can be observed at approximately the same positions through time (Figs. 12 and 13a,b), despite maximal displacements of up to 55 m between October 2008 and October 2009 (Niethammer et al., 2011a). This indicates the recurrent continuous in-situ formation where the fissures provide a close representation of the local strain field, similar as observed for the evolution of glacier crevasses (Harper et al., 1998).

Previous studies (Malet, 2003; Niethammer et al., 2011a; Walter et al., 2012) already observed close relationships between the occurrence of fissures and the geometry of the stable bedrock at the Super-Sauze landslide. They also noted a general contrast between higher water

content and rather ductile behaviour in the lower subsurface (<1 m) and typically lower water content of the topsoil yielding more brittle behaviour at the surface. The surface fissures can therefore be understood as the response to stresses induced in the topsoil through coupling with ductile strain in the deeper subsurface. A similar model was already described by Fleming and Johnson (1989) and adopted as a basis to qualitatively estimate the patterns of flow and stresses from a joint-interpretation (Fig. 13) of the detected fissure patterns and a geometrical model of the stable bedrock (Travelletti and Malet, 2012).

Considering the bedrock geometry and a formation of the open fissures normal to the direction of the least compressive stress (Pollard and Fletcher, 2005), three different flow field patterns leading to the fissure formation at the Super-Sauze landslide can be suggested. First, lateral shear at external and internal landslide boundaries aligned with the general flow field leads to the formation of diagonal shear fissure arrays (Fig. 13e). Second, longitudinal compressive and tensile strain related to abrupt changes in the slope of the sliding surface induces tensile stresses at the surface that results in transversal fissure arrays (Fig. 13c). Third, divergence of the flow field over topographic ridges and at the outlets of confining topographic channels induces lateral extension and tensile stresses resulting in longitudinal fissure arrays (Fig. 13d). At several locations, those processes overlap and lead to the formation of mixed structures such as a radial fissure patterns displayed in Figs. 4 and 13c, resulting from lateral shear and longitudinal strain, and from a divergent stress field, respectively.

### 5.3. Accuracy and related uses

Deformation patterns at the surface of landslides are important indicators for the mechanical processes, whereas the elaboration of detailed maps of such features remains a challenging and time-consuming task. While Sowers and Royster (1978) still argued that aerial photographs do not reach sufficient resolution for such mappings, modern digital sensors and new aerial platforms such as UAVs today provide the necessary level of detail. Furthermore, this study demonstrated the possible use of a semi-automatic image processing chain for the extraction of surface fissure maps.

The accuracy of the method was assessed by comparisons with expert maps and demonstrated heterogeneous areal accuracies with true positive rates of up to 65% and false positive rates generally below 10%. In addition, the orientation accuracy showed a variable quality of the resulting maps with mean deviations between 9.7° and 22.5°. The fissure densities derived from both maps have significant correlations ($R^2 = 0.36–0.78$), whereas the semi-automatic detections yield typically higher estimates. Interestingly, this difference is more pronounced with the images of 2009 (Fig. 10) reflecting the contrast between increased semi-automatic detection rates at higher resolutions and the fixed scale of the expert mapping. Contrariwise, the best agreement among detection and expert maps was measured for the scene of May 2007 showing that the lower resolution does not necessarily yield lower accuracies. Generally, lower accuracies were observed for the scenes recorded with full sunlight at the surface in July 2008 and 2009, and the worst results were obtained for July 2008 when images were recorded at a relatively low sun incidence angle. Since the direct sunlight induces shading that affects the local contrast and global image normalization methods cannot alleviate this problem, image acquisition with diffuse skylight appears to be the generally better option.

In the initial stage of the processing chain, a low-level linear feature detector is used. Similar techniques yield competitive results in medical image analysis (Zhang et al., 2010), whereas the accuracies achieved with aerial images in this study are still significantly lower. This must be attributed to the generally higher complexity of outdoor scenes and at the moment still requires additional steps and parameters to take the contextual scene information into account. The use of an OOA heuristic-based post-processing technique proved useful for the removal of false positives and helped to objectify the image analysis by transferring expert knowledge in an explicit form. The analysis still relies on a number of fixed thresholds which may hinder an easy transfer of the entire processing chain to a different geographic area. This concerns especially parameters that require knowledge of the local processes (e.g. minimum fissure length and effective friction angle), while thresholds that can be determined directly from the image (e.g. shadows and vegetation) may be adjusted more effortlessly.

The development of surface fissures precedes and accompanies especially slow- and very slow-moving landslides (Cruden and Varnes, 1996) making the developed technique particularly applicable to such types of landslides and to potentially unstable slopes. However, the spatial resolution of the acquired images must at least match, or should ideally exceed, the width of the targeted fissures, and the vegetation must be sufficiently sparse to permit direct view on the bare ground. The results of this study demonstrate that if those requirements are met, the obtained fissure maps can already provide sufficient accuracy to infer the landslide dynamics and mechanical processes at the slope scale (see Section 5.2). Density maps from both semi-automatic and expert mappings show a strong spatial and temporal variability of the fissure abundance pointing toward important local and temporal contrasts in the infiltration capacity which may need considerations in the design of hydro-mechanical models. An analysis of the evolution and mechanics of individual fissures will however require higher temporal resolution and terrestrial cameras have recently been installed at the surface of the landslide to record imagery for further research in this direction. It would also be desirable to test the developed technique for the investigation of other landslides with different characteristics in order to validate a more general applicability of the approach and the mechanical interpretation of the observed fissure dynamics.

The OOA heuristics already considers multi-scale information to some degree (see Section 4.3), whereas for further methodological improvements an explicit integration of an automatic scale selection technique at the low-level filtering stage appears as a promising approach to further reduce heuristics and tuneable parameters (Stumpf et al., 2012). The first and second stages of the proposed method are generic for the detection of dark linear features, and could in principle also be applied to detect other geomorphological and geological structures with similar characteristics. The proposed technique might be of interest for the mapping of gullies (Shruthi et al., 2011), geological lineaments (Mallast et al., 2011), ice-glacier crevasses (Vaughan, 1993) or tectonically induced fractures (Allmendinger and González, 2010), sufficiently larger to be depicted in sub-metre satellite images.

Considering the intrinsic disagreement in expert mappings of linear features, especially in the inter- and extrapolation of lines (Sander et al., 1997), further studies should also include an assessment of the uncertainties of reference maps since their quality can strongly bias the evaluation of different alternative approaches (Lampert et al., submitted for publication).

## 6. Conclusions

This study developed an image processing chain to extract surface fissures from heterogeneous sets of VHR aerial images and tested the approach with a challenging multi-temporal set of images recorded at the Super-Sauze landslide for five different dates. The first two stages of the developed workflow combine families of Gaussian matched filters and morphological filters, and are followed by an object-oriented analysis to reduce the amount of false positive detection using contextual information and auxiliary topographic information. The detection results can be represented in raster maps or optional by centre skeleton lines.

Under homogenous illumination conditions a comparison of the results with expert mapping demonstrated detection rates of up to 65% and orientation errors below 10°. Contrary, the technique is relatively sensitive to shading effects at full sunlight and prone to errors especially at low sun incidence angle. A joint-interpretation of obtained fissure

maps and of a 3D geometrical model of the stable bedrock demonstrated their complementary use for a better understanding of the geomorphological and geomechanical processes, such that the detected fissure pattern may be used for first approximation for mechanical processes in the recent deformation history of a slope. Possible directions for further research are the reduction of tuneable parameters and a more immediate exploitation of multi-scale information, as well as an adaption of the technique to other linear features with geomorphological and geological relevance.

## Acknowledgements

The work was supported by the project SafeLand "Living with landslide risk in Europe: assessment, effects of global change, and risk management strategies" funded by the 7th Framework Programme of the European Commission (grant agreement no. 226479), the project SISCA 'Système Intégré de Surveillance de Crises de Glissements de Terrain' funded by the French Research Agency (contract ANR Risk-Nat, 2009–2012), the project FOSTER 'Spatio-temporal data mining: application to the understanding and monitoring of soil erosion' funded by the French Research Agency (contract ANR Cosinus, 2011–2013), and the project Grosshang "Coupling of Flow and Deformation Processes for Modeling the Movement of Natural Slopes" funded by the Deutsche Forschungsgemeinschaft (DFG). The authors would like to acknowledge Alexandre Mathieu (University of Strasbourg) for his assistance in the field and for the expert mapping of the different fissure patterns, and Julien Travelletti for discussion on the recent dynamics of the landslide. The IDL code implementing the first two detection stages and the eCognition rule set implementing the object-oriented analysis are available on demand.

## References

Abramson, L.W., Lee, T.S., Sharma, S., Boyce, G.M., 2001. Slope Stability and Stabilization Methods, 2nd edition. Wiley, Chichester.
Allmendinger, R.W., González, G., 2010. Invited review paper: Neogene to Quaternary tectonics of the coastal Cordillera, northern Chile. Tectonophysics 495, 93–110.
Anderson, T.L., 2005. Fracture Mechanics: Fundamentals and Applications, 3rd edition. Taylor & Francis.
Ariza-López, F., Mozas-Calvache, A., 2012. Comparison of four line-based positional assessment methods by means of synthetic data. GeoInformatica 16, 221–243.
Backers, T., 2004. Fracture Toughness Determination and Micromechanics of Rock Under Mode I and Mode II Loading. PhD, Universität Potsdam, Potsdam.
Baruch, A., Filin, S., 2011. Detection of gullies in roughly textured terrain using airborne laser scanning data. ISPRS Journal of Photogrammetry and Remote Sensing 66, 564–578.
Bièvre, G., Jongmans, D., Winiarski, T., Zumbo, V., 2012. Application of geophysical measurements for assessing the role of fissures in water infiltration within a clay landslide (Trièves area, French Alps). Hydrological Processes 26, 2128–2142.
Bombard, J.-P., 1968. Une approche des problèmes posés par l'étude des mouvements de terrains. Thèse de Géologie, Faculté des Sciences de Grenoble, Grenoble, (in French).
Canny, J., 1986. A computational approach to edge detection. IEEE Transactions on Pattern Analysis and Machine Intelligence 8, 679–698.
Canty, M.J., Nielsen, A.N., 2008. Automatic radiometric normalization of multitemporal satellite imagery with the iteratively re-weighted MAD transformation. Remote Sensing of Environment 112, 1025–1036.
Chaudhuri, S., Chatterjee, S., Katz, N., Nelson, M., Goldbaum, M., 1989. Detection of blood vessels in retinal images using two-dimensional matched filters. IEEE Transactions on Medical Imaging 8, 263–269.
Chowdhury, R.N., Zhang, S., 1991. Tension cracks and slope failure. In: Chandler, R.J. (Ed.), Proceedings of the International Conference on Slope Stability Engineering: Developments and Applications. Institution of Civil Engineers, Isle of Wight, pp. 27–32.
Cruden, D.M., Varnes, D.J., 1996. Landslides types and processes. In: Turner, A.K., Schuster, R.L. (Eds.), Landslides: Investigation and Mitigation. Transportation Research Board, Special Report, 247. National Academy of Sciences, Washington, DC, pp. 36–75.
Davis, G.H., Reynolds, S.J., 1996. Structural Geology of Rocks and Regions. Wiley, Chichester.
Eisenbeiss, H., 2009. UAV Photogrammetry. PhD, ETH Zürich, Zürich.
Espinosa, A., 2009. Analysis and Quantification of Preferential Flow on the Super-Sauze Landslide. MSc, Delft University of Technology, Delft, Netherlands. (80 pp.).
Fleming, R.W., Johnson, A.M., 1989. Structures associated with strike–slip faults that bound landslide elements. Engineering Geology 27, 39–114.
Fleming, R.W., Baum, R.L., Giardino, M., 1999. Map and description of the active part of the slumgullion landslide, Hinsdale County, Colorado. Geologic Invstigations Series Map I-2672. U.S. Geological Survey, Denver, Colorado.
Frost & Sullivan Co., 2007. Study analysing the current activities in the field of UAV. European Comission Enterprise and Industry Directorate-General.
Glenn, N.F., Streutker, D.R., Chadwick, D.J., Thackray, G.D., Dorsch, S.J., 2006. Analysis of LiDAR-derived topographic information for characterizing and differentiating landslide morphology and activity. Geomorphology 73, 131–148.
González, R.C., Woods, R.E., 2008. Digital Image Processing, 3rd edition. Prentice Hall, Upper Saddle River.
Gotway, C.A., Young, L.J., 2002. Combining incompatible spatial data. Journal of the American Statistical Association 97, 632–648.
Graham, D.J., Rollet, A.-J., Piégay, H., Rice, S.P., 2010. Maximizing the accuracy of image-based surface sediment sampling techniques. Water Resources Research 46 http://dx.doi.org/10.1029/2008WR006940.
Grandjean, G., Bitri, A., Krzeminska, D.M., 2011. Characterisation of a landslide fissure pattern by integrating seismic azimuth tomography and geotechnical testing. Hydrological Processes 26, 2120–2127.
Günther, A., Carstensen, A., Pohl, W., 2004. Automated sliding susceptibility mapping of rock slopes. Natural Hazards and Earth System Sciences 4, 95–102.
Harper, J.T., Humphrey, N.F., Pfeffer, W.T., 1998. Crevasse patterns and the strain-rate tensor: a high-resolution comparison. Journal of Glaciology 44, 68–76.
Hoek, E., Bray, J.W., 1981. Rock Slope Engineering. The Institution of Mining and Metallurgy, London.
Hong, G., Zhang, Y., 2008. A comparative study on radiometric normalization using high resolution satellite images. International Journal of Remote Sensing 29, 425–438.
Hoover, A.D., Kouznetsova, V., Goldbaum, M., 2000. Locating blood vessels in retinal images by piecewise threshold probing of a matched filter response. IEEE Transactions on Medical Imaging 19, 203–210.
Jaboyedoff, M., Baillifard, F., Couture, R., Locat, J., Locat, P., 2004. Toward preliminary hazard assessment using DEM topographic analysis and simple mechanical modeling by means of sloping local base level. In: Lacerda, W.A., Ehrlich, M., Fontoura, A.B., Sayão, A. (Eds.), Landslides: Evaluation and Stabilization. Taylor & Francis Group, London, pp. 199–205.
Jammalamadaka, S.R., SenGupta, A., 2001. Topics in Circular Statistics. World Scientific, Singapore.
Ke, C.C., Chen, C.S., Tu, C.H., 2008. Determination of fracture toughness of anisotropic rocks by boundary element method. Rock Mechanics and Rock Engineering 41, 509–538.
Khattak, G.A., Owen, L.A., Kamp, U., Harp, E.L., 2010. Evolution of earthquake-triggered landslides in the Kashmir Himalaya, northern Pakistan. Geomorphology 115, 102–108.
Krauskopf, K.B., Feitler, S., Griggs, A.B., 1939. Structural features of a landslide near Gilroy, California. Journal of Geology 47, 630–648.
Krzeminska, D.M., Bogaard, T.A., van Asch, T.W.J., van Beek, L.P.H., 2011. A conceptual model of the hydrological influence of fissures on landslide activity. Hydrology and Earth System Sciences 8, 11039–11073.
Lampert, T.A., O'Keefe, S.E.M., 2011. A detailed investigation into low-level feature detection in spectrogram images. Pattern Recognition 44, 2076–2092.
Lampert, T.A., Stumpf, A., Gancarski, P., submitted for publication. An empirical study into expert agreement and ground truth estimation. IEEE Conference on Computer Vision and Pattern Recognition, Portland, USA.
Malet, J.P., 2003. Les 'glissements de type écoulement' dans les marnes noires des Alpes du Sud. Morphologie, fonctionnement et modélisation hydro-mécanique. PhD, Université Louis Pasteur, Strasbourg (in French).
Malet, J.-P., Auzet, A.-V., Maquaire, O., Ambroise, B., Descroix, L., Esteves, M., Vandervaere, J.-P., Truchet, E., 2003. Soil surface characteristics influence on infiltration in black marls: application to the Super-Sauze earth flow (southern Alps, France). Earth Surface Processes and Landforms 28, 547–564.
Malet, J.P., van Asch, T.W.J., van Beek, R., Maquaire, O., 2005a. Forecasting the behaviour of complex landslides with a spatially distributed hydrological model. Natural Hazards and Earth System Sciences 5, 71–85.
Malet, J.P., Laigle, D., Remaître, A., Maquaire, O., 2005b. Triggering conditions and mobility of debris flows associated to complex earthflows. Geomorphology 66, 215–235.
Mallast, U., Gloaguen, R., Geyer, S., Rödiger, T., Siebert, C., 2011. Semi-automatic extraction of lineaments from remote sensing data and the derivation of groundwater flowpaths. Hydrology and Earth System Sciences Discussions 8, 1399–1431.
Marr, D., Hildreth, E., 1980. Theory of edge detection. Proceedings of the Royal Society of London, Series B: Biological Sciences 207, 187–217.
Martha, T., Kerle, N., van Westen, C.J., Kumar, K., 2010. Characterising spectral, spatial and morphometric properties of landslides for semi-automatic detection using object-oriented methods. Geomorphology 116, 24–36.
Matheson, G.D., 1983. Rock Stability Assessment in Preliminary Site Investigations — Graphical Methods. Transport and Road Research Laboratory, Crownthorne.
McCalpin, J., 1984. Preliminary age classification of landslides for inventory mapping. 21st Annual Engineering Geology and Soils Engineering Symposium, Moscow, Idaho, pp. 99–111.
Meisina, C., 2006. Characterisation of weathered clayey soils responsible for shallow landslides. Natural Hazards and Earth System Sciences 6, 825–838.
Melton, F.A., 1959. Aerial photographs and structural geomorphology. Journal of Geology 67, 351–370.
Mendonca, A.M., Campilho, A., 2006. Segmentation of retinal blood vessels by combining the detection of centerlines and morphological reconstruction. IEEE Transactions on Medical Imaging 25, 1200–1213.
Metzger, W., 1975. Gesetze des Sehens, 3. Auflage. Waldemar Kramer, Frankfurt am Main.
Niethammer, U., Rothmund, S., James, M.R., Travelletti, J., Joswig, M., 2010. UAV-based remote sensing of landslides. ISPRS Commission V Mid Term Symposium XXXVIII, Part 5, pp. 496–501.
Niethammer, U., James, M.R., Rothmund, S., Travelletti, J., Joswig, M., 2011a. UAV-based remote sensing of the Super-Sauze landslide: evaluation and results. Engineering Geology 128, 2–11.

Niethammer, U., Rothmund, S., Schwaderer, U., Zeman, J., Joswig, M., 2011b. Open source image-processing tools for low cost UAV-based landslide investigations. The International Archives of the Photogrammetry, Remote Sensing and Spatial Information Sciences XXXVIII-1/C22.
Otsu, N., 1979. A threshold selection method from gray-level histograms. IEEE Transactions on Systems, Man, and Cybernetics 9, 62–66.
Papari, G., Petkov, N., 2011. Edge and line oriented contour detection: state of the art. Image and Vision Computing 29, 79–103.
Parise, M., 2003. Observation of surface features on an active landslide, and implications for understanding its history of movement. Natural Hazards and Earth System Sciences 3, 569–580.
Passchier, C.W., Trouw, R.A.J., 2005. Microtectonics. Springer, Berlin Heidelberg.
Pollard, D.D., Fletcher, R.C., 2005. Fundamentals of Structural Geology. Cambridge University Press, New York. Third printing with corrections.
Prats, X., Ramírez, J., Delgado, L., Royo, P., 2012. Regulations and requirements. In: Angelov, P. (Ed.), In Sense and Avoid in UAS: Research and Applications. Wiley, Chichester, pp. 87–117.
Priest, S.D., 1993. Discontinuity Analysis for Rock Engineering. Chapman & Hall, London.
Quackenbush, L.J., 2004. A review of techniques for extracting linear features from imagery. Photogrammetric Engineering and Remote Sensing 70, 1383–1392.
Riedel, W., 1929. Zur Mechanik geologischer Brucherscheinungen. Zentralblatt für Mineralogie, Geologie und Paläontologie B 354–368.
Sander, P., Minor, T.B., Chesley, M.M., 1997. Ground-water exploration based on lineament analysis and reproducibility tests. Ground Water 35, 888–894.
Schott, J.R., Salvaggio, C., Volchok, W.J., 1988. Radiometric scene normalization using pseudoinvariant features. Remote Sensing of Environment 26, 1–16.
Schulson, E.M., Duval, P., 2009. Creep and Fracture of Ice. Cambridge University Press, New York.
Selby, M.J., 1993. Hillslope Materials and Processes, 2nd edition. Oxford University Press, Oxford.
Serra, J., 1982. Image Analysis and Mathematical Morpholgy. Academic Press, Orlando.
Shao, Y., Guo, B., Hu, X., Di, L., 2011. Application of a fast linear feature detector to road extraction from remotely sensed imagery. IEEE Journal of Selected Topics in Applied Earth Observations and Remote Sensing 4, 626–631.
Shreve, R.L., 1966. Sherman landslide, Alaska. Science 154, 1639–1643.
Shruthi, R.B.V., Kerle, N., Jetten, V., 2011. Object-based gully feature extraction using high spatial resolution imagery. Geomorphology 134, 260–268.
Soares, J.V.B., Leandro, J.J.G., Cesar, R.M., Jelinek, H.F., Cree, M.J., 2006. Retinal vessel segmentation using the 2-D Gabor wavelet and supervised classification. IEEE Transactions on Medical Imaging 25, 1214–1222.
Sofka, M., Stewart, C.V., 2006. Retinal vessel centerline extraction using multiscale matched filters, confidence and edge measures. IEEE Transactions on Medical Imaging 25, 1531–1546.
Sowers, G.F., Royster, D.L., 1978. Field investigation. In: Schuster, R.L., Krizek, R.J. (Eds.), Landslides: Analysis and Control. Transportation Research Board, Special Report, 176. National Academy of Science, Washington, DC, pp. 81–111.
Stumpf, A., Kerle, N., 2011. Object-oriented mapping of landslides using Random Forests. Remote Sensing of Environment 115, 2564–2577.
Stumpf, A., Lampert, T.A., Malet, J.-P., Kerle, N., 2012. Multi-scale line detection for landslide fissure mapping. International Geoscience and Remote Sensing Symposium, Munich, Germany, p. 4.
Tarboton, D.G., Bras, R.L., Rodriguez-Iturbe, I., 1991. On the extraction of channel networks from digital elevation data. Hydrological Processes 5, 81–100.
Tchalenko, J.S., 1970. Similarities between shear zones of different magnitudes. Geological Society of America Bulletin 81, 1625–1640.
Ter-Stephanian, G., 1946. On the landslide cracks classification. Bulletin of the Academy of Sciences of the Armenian SSR 10, 65–80 (in Russian with abstracts in Armenian and English).
Travelletti, J., 2011. Imagerie multi-paramètres et multi-résolutions pour l'observation et la caractérisation des mécanismes de glissements-coulées. PhD, Université de Caen Basse-Normandie, Strasbourg.
Travelletti, J., Malet, J.P., 2012. Characterization of the 3D geometry of flow-like landslides: a methodology based on the integration of heterogeneous multi-source data. Engineering Geology 128, 30–48.
Trimble, 2011. eCognition Developer 8.64.0. Reference Book. Trimble Documentation, München.
Tveite, H., Langaas, S., 1999. An accuracy assessment method for geographical line data sets based on buffering. International Journal of Geographical Information Science 13, 27–47.
Vallet, J., 2007. GPS/IMU and LiDAR integration to aerial photogrammetry: development and practical experiences with Helimap System®, 27. Wissenschaftlich-Technische Jahrestagung der DGPF, Dreiländertagung, Muttenz.
van Asch, T.W.J., van Beek, L.P.H., Bogaard, T.A., 2009. The diversity in hydrological triggering systems of landslides. The First Italian Workshop on Landslides, Napoli, Italy, pp. 151–156.
Vaughan, D.G., 1993. Relating the occurrence of crevasses to surface strain rates. Journal of Glaciology 39, 255–266.
Vicente-Serrano, S.M., Pérez-Cabello, F., Lasanta, T., 2008. Assessment of radiometric correction techniques in analyzing vegetation variability and change using time series of Landsat images. Remote Sensing of Environment 112, 3916–3934.
Walter, M., Niethammer, U., Rothmund, S., Joswig, M., 2009. Joint analysis of the Super-Sauze (French Alps) mudslide by nanoseismic monitoring and UAV-based remote sensing. First Break 27, 53–60.
Walter, M., Arnhardt, C., Joswig, M., 2012. Seismic monitoring of rockfalls, slide quakes, and fissure development at the Super-Sauze mudslide, French Alps. Engineering Geology 128, 12–22.
Wang, E.Z., Shrive, N.G., 1995. Brittle fracture in compression: mechanisms, models and criteria. Engineering Fracture Mechanics 52, 1107–1126.
Watts, A.C., Ambrosia, V.G., Hinkley, E.A., 2012. Unmanned aircraft systems in remote sensing and scientific research: classification and considerations of use. Remote Sensing 4, 1671–1692.
Youssef, A., Maerz, N., Hassan, A., 2009. Remote sensing applications to geological problems in Egypt: case study, slope instability investigation, Sharm El-Sheikh/Ras-Nasrani area, southern Sinai. Landslides 6, 353–360.
Zhang, B., Zhang, L., Zhang, L., Karray, F., 2010. Retinal vessel extraction by matched filter with first-order derivative of Gaussian. Computers in Biology and Medicine 40, 438–445.